remote sensing

IMPACT FACTOR 5.0

CITESCORE 7.9

Article

Evaluating the Performance of Sentinel-3A OLCI Products in the Subarctic Northeast Pacific

Perumthuruthil Suseelan Vishnu and Maycira Costa

Special Issue

Advances of Remote Sensing on North Pacific Ecosystems, the Equatorial Pacific Band, and Adjacent Seas

Edited by

Dr. José C.B. da Silva, Prof. Dr. Caixia Wang and Dr. Jorge M. Magalhaes

MDPI

https://doi.org/10.3390/rs15133244

remote sensing

MDPI

Article

Evaluating the Performance of Sentinel-3A OLCI Products in the Subarctic Northeast Pacific

Perumthuruthil Suseelan Vishnu * and Maycira Costa

SPECTRAL Remote Sensing Laboratory, Department of Geography, University of Victoria, Victoria, BC V8P 5C2, Canada; maycira@uvic.ca

* Correspondence: psvishnu2014@gmail.com; Tel.: +1-250-813-1439

Abstract: The subarctic northeast Pacific (SNEP) is a high-nitrate, low-chlorophyll (HNLC) region in the ocean, where phytoplankton growth and productivity are limited by iron. Moreover, there is a limited application of high spatial (300 m) and temporal resolution (daily) ocean color (OC) satellite imagery in studying the phytoplankton dynamics in this region. To address this issue, we aim to validate the remote sensing reflectance (Rrs; $sr^{-1}(\lambda)$) and chlorophyll-a (Chla) concentration derived from the Polymer atmospheric correction algorithm against in situ data for the SNEP obtained during 2019 and 2020. Additionally, we performed qualitative analysis using weekly binned surface Chla maps to determine whether the product reflects the general pattern over a latitudinal and longitudinal domain. We processed the daily Level-1 image using Polymer and binned them weekly using Graphic Processing Tool (GPT). The validation results indicate that Polymer exhibits higher radiometric performance in the blue and green bands and fails to represent in situ Rrs in the red band. Furthermore, the Polymer slightly over- and underestimates reflectance between 0.0012 and 0.0018 sr^{-1} in the green band. On the other hand, excellent agreement was found between satellite-derived versus in situ Chla, followed by a slight overestimation of in situ Chla in the range from 0.17 to 0.28 mg/m^3. The weekly binned Chla spatial map revealed a spatially homogeneous distribution of surface Chla in Central Alaska, but a substantial increase in Chla ($\geq$0.7 mg/m^3) was recorded toward Southeast Alaska (SEA) and the British Columbia (BC) shelf. Furthermore, Chla derived from latitudinal and longitudinal transects indicates high Chla toward 57°N and −135°W, respectively. Overall, the results of this study emphasize the need to obtain high-quality matchups from under-sampled oligotrophic waters, which are crucial for satellite validation, in addition to highlighting the importance of using high spatial and temporal resolution satellite imagery to study phytoplankton dynamics in the SNEP.

Keywords: northeast Pacific Ocean; phytoplankton; chlorophyll-a; ocean color; remote sensing; OLCI Sentinel-3A

Citation: Vishnu, P.S.; Costa, M. Evaluating the Performance of Sentinel-3A OLCI Products in the Subarctic Northeast Pacific. *Remote Sens.* **2023**, *15*, 3244. https://doi.org/10.3390/rs15133244

Academic Editors: José C.B. da Silva, Jorge M. Magalhaes and Caixia Wang

Received: 29 April 2023
Revised: 16 June 2023
Accepted: 19 June 2023
Published: 23 June 2023

1. Introduction

Marine phytoplankton are essential for regulating Earth's climate and account for 50% of the global primary productivity [1–3]. Phytoplankton are highly diverse in size, shape, and taxonomic composition, exhibiting enormous diversity within a single species; for example, phytoplankton are found with different morphological and physiological characteristics and sometimes different life stages and ecological niches [4]. Thus, monitoring phytoplankton and assessing their shift in the ocean is paramount to determining the global carbon cycle, ocean biogeochemistry, implications for the marine food web, and how climate change will impact the ocean ecosystem.

This is especially relevant for the open ocean waters of the subarctic northeast Pacific (SNEP; Figure 1), a high-nutrient–low-chlorophyll (HNLC) region where iron is the limiting nutrient that regulates phytoplankton biomass and primary productivity [5–8]. Chlorophyll-a concentration (hereafter Chla, a proxy for phytoplankton biomass [9]) generally remains low in central Alaska at $\leq$0.5 mg/m^3; nevertheless, sporadic phytoplankton

bloom may occur in the HNLC region due to the introduction of iron [10]. This HNLC region extended through the central Pacific [6]; hence, phytoplankton blooms are generally absent during spring and summer [7]. However, this regular state may sometimes be altered by short-lived phytoplankton blooms during fall [8,11–13] as a result of the relaxation in grazing pressure from micro- and macrozooplankton, aerial iron deposition, or advection of nutrient-rich water from the shelf [11,14,15]. The Subarctic Ecosystem Response to Iron Enrichment (SERIES) experiment has clearly shown that iron ultimately limits the utilization of macronutrients and regulates new production during summer in the SNEP [16]. This has important implications for the open ocean waters of the SNEP, which are crucial for sustaining commercially important fisheries and supporting the population of Pacific Salmon originating from Canada, the United States, Japan, Korea, and Russia [17].

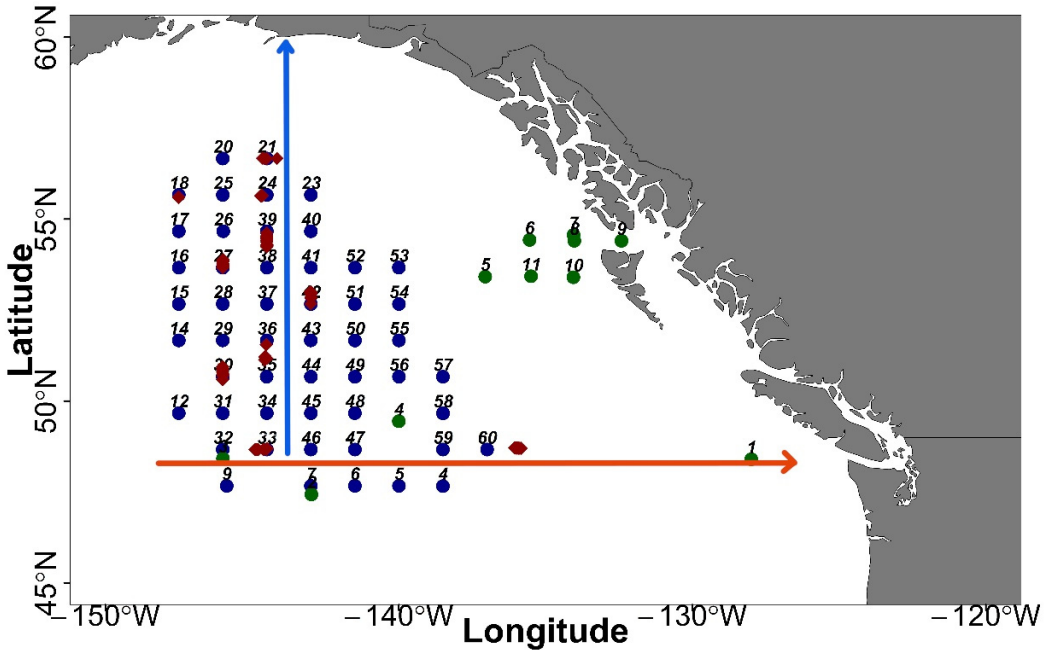

Figure 1. Study area map showing the sampling locations in 2019 and 2020. Circles indicate field stations and are shown in blue for 2019 and green for 2020. Red circles indicate the transect for the above-water radiometer operated in 2019. Chlorophyll-a concentrations were extracted from each weekly composite imagery over the latitudinal and longitudinal domains represented by the blue and red lines, respectively.

Similarly, the coastal and continental domains of SNEP are known for their high productivity and diverse marine life [18–24], including various marine mammals [19,20], commercially important fish species [18,21–23], and seabirds [24]. This high productivity is attributed, in part, to the variability of phytoplankton in this region [25,26]. Studies using both in situ measurements and satellite data have revealed high values of Chla (>3 mg m^{-3}) in the coastal waters along with phytoplankton blooms, showing pronounced seasonal, spatial, and interannual variability [27,28].

Monitoring the dynamics of ocean productivity and its implications for the food web, which is based on measuring the concentration and composition of phytoplankton in the ocean, is generally conducted using various in situ techniques, including flow cytometry, size-fractionated filtration (SFF), high-performance liquid chromatography (HPLC) pigment analysis, conventional imaging flow cytometry [29], Imaging FlowCytobot, genomics, and next-generation sequencing [30]. However, specifically for the SNEP, light-microscopy [31–33], HPLC pigment analysis [34], chemical taxonomy (CHEMTAX) software [35–39], and physical–biological models [40] have been implemented. These methods are extremely useful but are limited in time and space, and are often time-consuming, labor-intensive, and expensive [30,41]. Consequently, the availability of in situ phytoplank-

ton data becomes constrained, preventing the use of these datasets for monitoring the large-scale dynamics of phytoplankton and understanding how environmental drivers influence their spatiotemporal distribution.

To address this issue, space-based ocean monitoring using optical sensors can monitor the upper ocean ecosystem on a synoptic scale with a high spatial and temporal resolution that is often unattainable for ship-based observation [9]. Given the importance of determining phytoplankton dynamics over large spatiotemporal scales, several studies have used ocean color (OC) satellites to elucidate phytoplankton dynamics in the SNEP [6,7,12,27,42]. Indeed, most of these past studies have used OC sensors that have coarse spatial (4–25 km) resolution, and none have yet explored the potential of the new generation of OC sensors such as Ocean Land Color Instrument (OLCI) onboard Sentinel-3A satellite with high spatial (300 m) and temporal resolution (<1.4 days) [43].

Here, we evaluate the performance of satellite-derived remote sensing reflectance (Rrs; $sr^{-1}(\lambda)$) and chlorophyll-a concentration in the SNEP, specifically during 2019 and 2020. The satellite product was mainly produced using the POLYnomial-based algorithm applied to MERIS (Polymer) and the European Space Agency Baseline Atmospheric Correction (BAC) algorithm, and its performance was then assessed via statistical validation against in situ measurements. Additionally, we conducted a qualitative analysis to discuss whether the satellite data reflect the region's latitudinal and longitudinal dynamics. The evaluation of the OLCI product derived from multiple processors across the global and regional waters is a critical step in the process of Sentinel-3 OLCI validation, and here we are providing the first reported analysis for the northeast Pacific region.

2. Materials and Methods

2.1. Study Area

The circulation in central Alaska is primarily driven by the counterclockwise-flowing Subarctic Gyre, consisting of three components: the North Pacific Current, the Alaska Current, and the Alaska Stream [44]. The Alaska Stream is a high-speed current characterized by eddies and meanders, flowing southwestward parallel to the coast of Alaska. It connects to the North Pacific Current at 170°W, completing the Subarctic Gyre [44,45]. This oceanographic region (Figure 1) is classified as an HNLC area with abundant nitrate concentrations and moderate primary productivity throughout the year due to limited iron availability [46,47]. The primary productivity in the region fluctuates annually between 5 and 18 mol C m^{-2} yr^{-1} [48], whereas the concentrations of Chla in the region exhibit no seasonal or interannual variability, with values $\leq$ 0.5 mg/m^3 [6,46–50]. This pattern has been confirmed by remote sensing of the surface Chla and recent observations from the Biogeochemical Argo float (BGC-Argo) deployed in the SNEP, which recorded low variability in Chla concentrations of the upper ocean between 0 and 150 m [40]. The dominant phytoplankton community in the open ocean region consists of small-sized nano- and picophytoplankton, such as haptophytes, followed by green algae and pelagophytes [31,36,37,39], whereas large-sized microphytoplankton, such as diatoms, contribute little to the total biomass in this region [36,39].

In contrast, the coastal waters of southeast Alaska (SEA) and British Columbia (BC) are highly productive and rich in marine life, providing habitats for commercially important fish species such as Pacific Cod, Walleye Pollock, Pacific Ocean Perch, and Pacific Herring [18,21–23], as well as several species of marine mammals [19,20] and seabirds [24]. Despite being a downwelling-dominated region throughout the year, the coastal waters of SEA exhibit exceptional productivity, with annual primary productivity surpassing 300 g C m^{-2} y^{-1} [25]. The Alaska Coastal Current (ACC), driven by wind and freshwater runoff, dominates this region and is responsible for transporting dissolved organic matter, phytoplankton, zooplankton, and other marine organisms northwards to the Bering Sea [51]. On the other hand, the BC coast serves as a transitional zone between the strong downwelling-dominated region in SEA and the upwelling-dominated coastal region in southern California [45]. This region serves as the primary marine entry point for many

Pacific Salmon species, with the majority of juvenile Sockeye Salmon leaving the Salish Sea during summer and fall and entering the Gulf of Alaska (GoA) through these coastal waters [52]. Phytoplankton biomass undergoes annual cycles, with extensive spring diatom blooms observed along the SEA and BC coasts [27,53,54]. Diatoms are the dominant bloom-forming community in this region, and Chla concentrations typically exceed 3 mg/m^3 during the spring bloom, dominated by *Skeletonema costatum*, *Chaetoceros* spp., and *Thalassiosira* spp. [7,13,27,54].

2.2. Datasets

The following dataset was compiled for this study: above-water reflectance measurements were acquired to validate satellite-derived reflectance, and discrete water samples collected from the surface ocean were analyzed for HPLC pigments to validate the satellite-derived Chla product. Additionally, qualitative analysis was conducted using weekly binned surface Chla composites generated from atmospheric-corrected daily OLCI imagery to determine the gradients of the region's latitudinal and longitudinal dynamics in the data. The following section presents the methods followed in this study.

2.3. In Situ Data

The in situ datasets used in this study (Figure 1) were collected as part of the International Year of Salmon (IYS) expedition to the Gulf of Alaska from 18 February to 21 March 2019 and from 5 March to 5 April 2020. The 2019 expedition was onboard R/V *Professor Kaganovsky*, while the 2020 expedition was onboard R/V *Pacific Legacy*. The datasets derived from these expeditions were utilized to perform one-to-one matchup analysis to determine the accuracy of Sentinel-3 OLCI product over the surface waters of the SNEP region. This section is organized as follows: first, we describe the methods used for processing in situ and satellite data; second, we present the validation of satellite-derived Rrs(λ) and Chla; finally, we qualitatively assess how well the weekly binned OLCI Chla map reproduces the regional pattern over a latitudinal and longitudinal domain.

2.3.1. Phytoplankton Pigment Analysis

From the expeditions, surface water samples for phytoplankton pigment analysis were collected using CTD/rosette from approximately 5 m. Water samples were then transferred to a 10 L plastic container and transported to the laboratory with immediate initiation of onboard filtration, which was conducted in the dark to avoid potential pigment degradation [55]. Surface water samples of 1–2 L from each station, for the duplicate measurement of HPLC pigment analysis, were filtered through a 25 mm Whatman GF/F 0.7 µm glass microfiber filter under low light conditions and low vacuum ($\leq$5 mmHg). After filtration, the filters were flash-frozen in liquid nitrogen and immediately kept at -20 °C until analysis in the laboratory. The filter was then extracted with methanol and analyzed using a well-calibrated Shimadzu HPLC instrument [56]. The HPLC pigment analysis was conducted at the University of South Carolina Baruch Institute of Marine and Coastal Science (https://phytoninja.com/lab-protocols/, accessed on 10 April 2023), and the method was detailed in Pinckney 2010 [56]. Out of the 54 samples, 20% had duplicates, and the uncertainty in these duplicate samples was estimated based on a coefficient of variation (CV) < 20%. Finally, Chla concentration in the surface waters of the SNEP varied from 0.17 to 0.52 (0.35 $\pm$ 0.08 mg/m^3).

2.3.2. In Situ Remote Sensing Reflectance

Above-water spectral reflectance measurements were acquired during good weather conditions using a manually operated radiometer (HyperSAS) to evaluate OLCI-derived Rrs(λ) [57]. HyperSAS was only operated during the 2019 expedition (N = 43) due to logistic constraints in the 2020 expedition. HyperSAS consists of three hyperspectral radiometers, including sea surface radiance Lt(λ), sky radiance Li(λ), and a third sensor to measure total irradiance Es(λ); from these measurements, Rrs(λ) is derived [57]. HyperSAS was

installed on the bow of the R/V *Professor Kaganovsky* at a 13 m height from the sea surface to avoid the infrastructure shadows and spray. Specifically, Lt(λ) and Li(λ) sensors are at a fixed-viewing zenith angle, θv = 50°, and viewing sun azimuth, φv = 120°, to avoid glint effects [57,58]. The ideal φv is maintained by looking at the sun's position in the sky. Measurements were acquired between 11 a.m. and 2 p.m. to mimic the time of Sentinel-3A acquisition and optimized sun illumination conditions. Radiometric measurements were limited to a solar zenith angle of less than 60° [58] to limit variability in the water-leaving radiance. The data from the HyperSAS were processed using ProSoft version 7.7.19 to calculate Rrs(λ).

The above-water Rrs(λ) was calculated according to [59].

$$\mathbf{Rrs(\lambda)} = \frac{\mathbf{Lt(\lambda) - \rho s Li(\lambda)}}{\mathbf{Es(\lambda)}}, \left(\mathbf{sr^{-1}}\right) \quad (1)$$

where Lt(λ) is the total measured radiance by the sea-viewing sensor and ρs fraction of sky radiance measured by the sea-viewing sensor [59]. ρs is estimated according to the following equations [60].

$$\boldsymbol{\rho s = 0.0256 + 0.00039W + 0.000034W^2, \ when} \ \frac{\mathbf{Li\ (750nm)}}{\mathbf{Es\ (750nm)}} < \mathbf{0.05} \quad (2)$$

$$\boldsymbol{\rho s = 0.0256, \ when} \ \frac{\mathbf{Li\ (750nm)}}{\mathbf{Es\ (750nm)}} \geq \mathbf{0.05} \quad (3)$$

NIR (near-infrared) correction was applied to the reflectance spectra by subtracting the value at 750 nm following the method described in [60]. The final Rrs(λ) was derived from the quality-controlled in situ hyperspectral Rrs(λ) (hereafter Rrs in situ) subjected to the spectral response function (SRF) according to the spectral characterization of OLCI (https://sentinel.esa.int/web/sentinel/user-guides/sentinel-3-olci, accessed on 5 April 2023).

2.4. Sentinel-3A OLCI Data and Atmospheric Correction

The Ocean Land Color Instrument (OLCI) onboard the Sentinel-3A satellite provides high spatial (300 m) and temporal resolution ocean color data, and it operates in 10 spectral bands (400, 412, 443, 490, 510, 560, 620, 665, 674, and 681 nm) within the visible spectrum [61]. The sensor also features an improved signal-to-noise ratio (SNR) and an off-nadir pointing of the instrument swath to minimize the sunglint effect [61]. Therefore, for this study, OLCI Sentinel-3A Level-1 full-resolution data acquired during 2019 and 2020 (18 February to 21 March 2019, and from 5 March to 5 April 2020, corresponding to the fieldwork period) were downloaded from Sentinel-3 Marine CODA (Copernicus Online Data Access) web service and processed using Polymer version 4.10 to obtain Rrs(λ) and Chla (mg/m^3) following [62]. Polymer is a spectral matching algorithm that employs two models. Firstly, a polynomial function utilizes the full spectrum to model the spectral reflectance of the atmosphere and the residual sunglint contribution [63]. Secondly, the water reflectance model is based on Chla and a coefficient (fb), which scales the total backscattering coefficient of marine particles (bbp) [63]. The parameters in the atmospheric and water reflectance models are optimized through an iterative process to achieve the best spectral fit for the total reflectance received by the sensor [63]. Chla is a direct output of Polymer and is derived as part of the optimization scheme [63]. Specifically, Chla in the water reflectance models is derived from known measurements from various oceanic regions, rather than through a semi-analytical or bio-optical model [63]. It has been shown that Polymer water reflectance is applicable in both Case-1 and Case-2 water types [63]. This algorithm was originally developed for Medium Resolution Imaging Spectrometer (MERIS) and later adapted to other OC sensors such as Moderate Resolution Imaging Spectroradiometer (MODIS), Sea-viewing Wide Field-of-view Sensor (SeaWiFS), Visible Infrared Imaging Radiometer Suite (VIIRS), and OLCI. In this study, daily Level-1 data were downloaded and processed with Polymer and then binned into four composites

using SNAP (version 6.0) in batch mode using GPT (Graphics Processing Tool). While binning, the following quality flags of "Cloud", "Invalid", "Negative Backscattering (BB)", "Out-of-bounds", "Exception", "High Air Mass", and "Thick Aerosol" were applied based on the recommendation from [64] following [62], and the median Rrs(λ) calculated from each band was used for the analysis. Overall, eight composites were generated for 2019 and 2020. To obtain higher spatial coverage OC data for the open ocean, spatially and temporally binned 8-day composite maps were employed [65]; this is especially valid for Alaska's iron-poor open ocean waters, where Chla concentration exhibited subtle variability throughout our investigation (0.38 ± 0.08 mg/m^3) [39,40,46]. Along with Polymer (version 4.10), we tested the 8-day composite map of Level-2 Rrs(λ) and Chla distributed by the European Space Agency (ESA) to define the best processor for this region. The ESA Level-2 Rrs(λ) product is derived using the BAC algorithm [66], which was initially developed for MERIS by Antoine and Morel [67] and assumes there is no reflectance in the NIR part of the spectrum. Hence, the Chla and Rrs(λ) products are only valid for the global open ocean waters, where phytoplankton pigments dominate the signal. Later, BAC was integrated with the Bright Pixel Atmospheric Correction (BPAC) proposed by Moore et al. (1999) [68] and Moore et al. (2017) [69]. BPAC can account for high scattering waters dominated by high Chla and total suspended matter (TSM), where NIR reflectance is not zero. However, the initial validation results of satellite-derived Rrs(λ) (hereafter Rrs-satellite) showed poor radiometric performance at 443 (r = −0.42, MAE = 0.003 sr^{-1}, MDPD = 44.99%, BIAS = 12.51%), 560 (r = −0.23, MAE = 0.0006 sr^{-1}, MDPD = 33.55%, BIAS = 11.67%), and 665 nm (r = 0.00, MAE = 0.0002 sr^{-1}, MDPD = 59.93%, BIAS = 52.04%). Similarly, Chla derived from the ESA Level-2 product for the 2019 dataset also showed poor statistical performance (r = 0.3, MAE = 0.08 mg/m^3, MDPD = 19.31%, BIAS = −2.74%) compared to Polymer. In addition, we observed a significant reduction (about 60%) of the valid data points when utilizing the ESA Level-2 product. Furthermore, due to clouds, the spatial coverage was substantially reduced during the expedition in the middle of winter in Alaska. However, we also noticed that the Polymer-processed Level-2 image provided much better spatial coverage compared to the ESA Level-2 product. Our observations are consistent with the latest study by Tilstone et al. 2021 [70], where Polymer-derived Chla reportedly showed the highest number of valid pixels and higher spatial coverage than other AC algorithms across the Atlantic Ocean, and that for the northeast Pacific by Giannini et al. 2021 [62]. Due to the design of the POLYMER processor, it is capable of retrieving the signal under sky glint conditions and thin clouds [64], thus allowing for extensive spatial coverage. As a result, we decided to conduct the entire validation utilizing Polymer. Finally, the Level-2 processed imagery from Polymer was cropped to the region of interest using Graph Processing Tool (GPT) of the Sentinel Application Platform (SNAP), specifically the "Subset" function. The resulting cropped imagery was then visualized using the "Raster" package in R [71].

2.5. Matchup Analysis: OLCI Rrs and Chla

The performance of the POLYMER AC algorithm was evaluated by conducting a one-to-one matchup analysis between satellite and in situ data. The Rrs satellite from the daily imagery was extracted from a 5 × 5-pixel window centered on the exact location of the Rrs in situ. Mean, median, and coefficient of variation (CV) were calculated for each matchup using the following criteria: ±5 h, valid pixels must be ≥17/25, CV at 560 nm must be ≤20%, and the median value from each band was used to avoid outlier [72–74].

The performance of OLCI-Chla retrievals was assessed based on the combined data from 2019 and 2020. For each in situ sample, satellite Chla was extracted from the 8-day composite imagery, and the mean, median, and CV were calculated for the Chla matchup using similar criteria as for the Rrs in situ [72–74]. We achieved a higher number of points using the 8-day composite imagery for both 2019 and 2020. In addition, the statistical performance was also highly comparable to that of the daily matchups.

The statistical error metrics such as r, mean absolute error (MAE), median percentage error (MDPD), and bias (BIAS) were obtained to evaluate the performance of Polymer AC algorithms [62]. The equation of MAE, MDPD, and BIAS are expressed as follows.

$$\mathbf{MAE} = \sum_{\mathbf{i=1}}^{\mathbf{i=N}} |(\mathbf{Sat_i} - \mathbf{Insitu_i})| \quad (4)$$

$$\mathbf{MDPD} = \mathbf{Median\ value\ of\ 100} \times \left| \frac{\mathbf{Sat_i} - \mathbf{Insitu_i}}{\mathbf{In\ situ_i}} \right| \quad (5)$$

$$\mathbf{Bias} = \sum_{\mathbf{i=1}}^{\mathbf{i=N}} \frac{(\mathbf{Sat_i} - \mathbf{Insitu_i})}{\mathbf{In\ situ_i}} \times \mathbf{100} \quad (6)$$

where Sat_i is the satellite-derived measurements, $Insitu_i$ is the in situ-derived measurements, and N is the number of observations.

Finally, a weekly trend analysis was conducted to evaluate the accuracy of satellite-derived Chla over a broad spatial scale. The trends are extracted across a latitudinal and longitudinal domain from a 5 × 5 window within each 8-day composite imagery, and the corresponding standard deviation is presented.

3. Results

3.1. Remote Sensing Reflectance Validation

Rrs in situ and Rrs satellite demonstrated a typical open ocean water spectrum [70], characterized by a maximum blue reflectance that decreased toward longer wavelengths and a Chla fluorescence peak near 680 nm (Figure 2). Rrs in situ and Rrs satellite for various bands (443, 560, and 665 nm) showed comparable dynamic ranges (Figure 3). Specifically, the average values at the 443, 560, and 665 nm bands were comparable between Rrs in situ and Rrs satellite, with values of 0.0049 ± 0.0009, 0.0048 ± 0.0005, 0.0018 ± 0.0003 and 0.0016 ± 0.0003, 0.00024 ± 0.00007, 0.00025 ± 0.00003, respectively. A detailed quantitative analysis demonstrated that the accuracy of Polymer AC varies with wavelength, where the correlation decreases with increasing wavelength (Figure 4). A highly significant ($p < 0.001$) correlation of 0.73 was obtained for 443 nm, followed by the best statistical performance (BIAS = 0.22%, MDPD = 7.97%; Figure 4). Similarly, a highly significant ($p < 0.001$) correlation of 0.50 was found for 560 nm, followed by a moderate statistical performance (BIAS = −13.09%, MDPD = 17.08%; Figure 4). For Rrs satellite at 560 nm, values < 0.0015 sr^{-1} were slightly overestimated, and Rrs between 0.0015 and 0.0018 sr^{-1} were underestimated. Finally, a poor correlation of −0.2 and decreased statistical metrics were obtained for 665 nm (BIAS = 11.82%, MDPD = 25.47%; Figure 4). Overall, Rrs satellite demonstrated the highest overestimation at 665 nm (BIAS = 11.82%), followed by the highest underestimation at 560 nm (BIAS = −13.09%). Similarly, the highest MDPD was observed at 665 nm (25.47%), followed by 560 nm (17.08%) and 443 nm (7.97%). On the other hand, the MAE was lower for all three bands (<4 × 10^{-4} sr^{-1}).

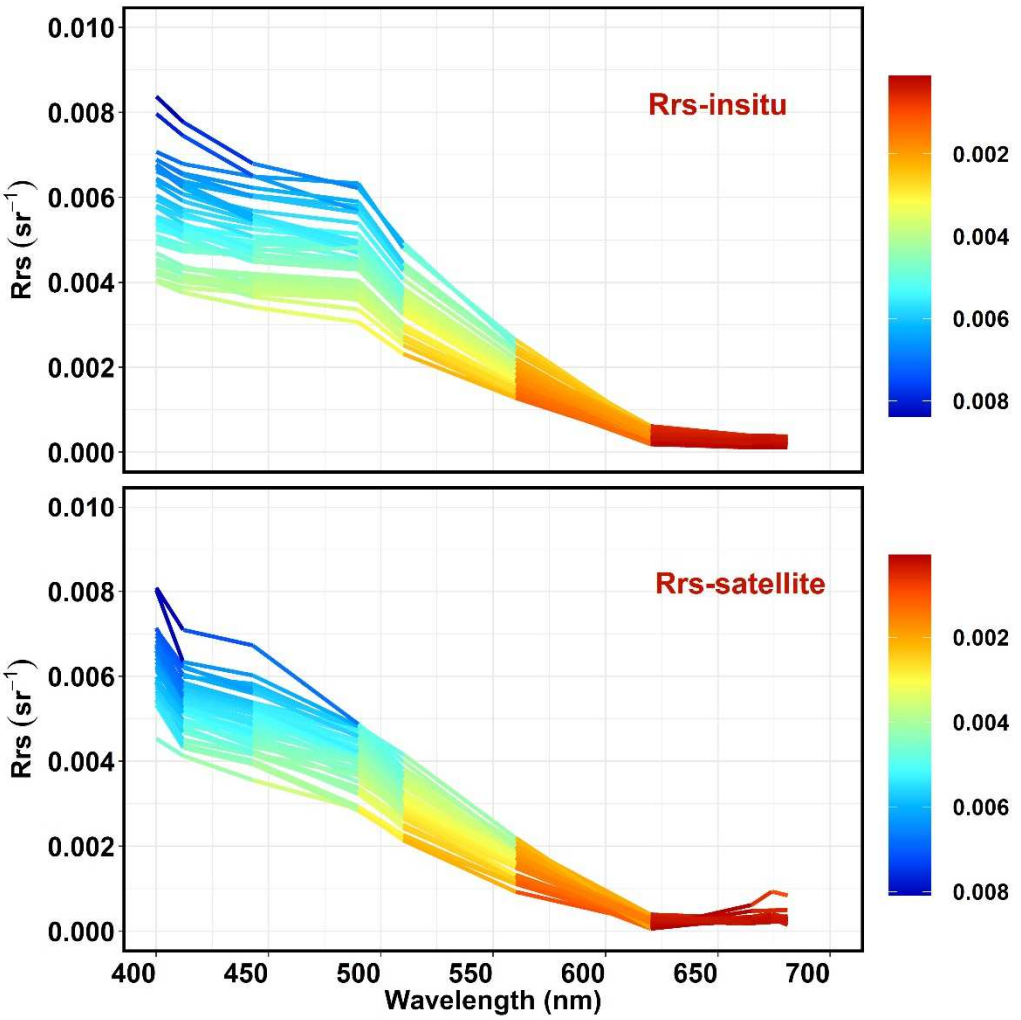

Figure 2. The diagram illustrates the simulated remote sensing reflectance spectra from the in situ hyperspectral remote sensing reflectance (Rrs in situ) in the top panel and the corresponding OLCI remote sensing reflectance spectra (Rrs satellite) in the bottom panel. Rrs satellite represents the median value from a 5 × 5-pixel window.

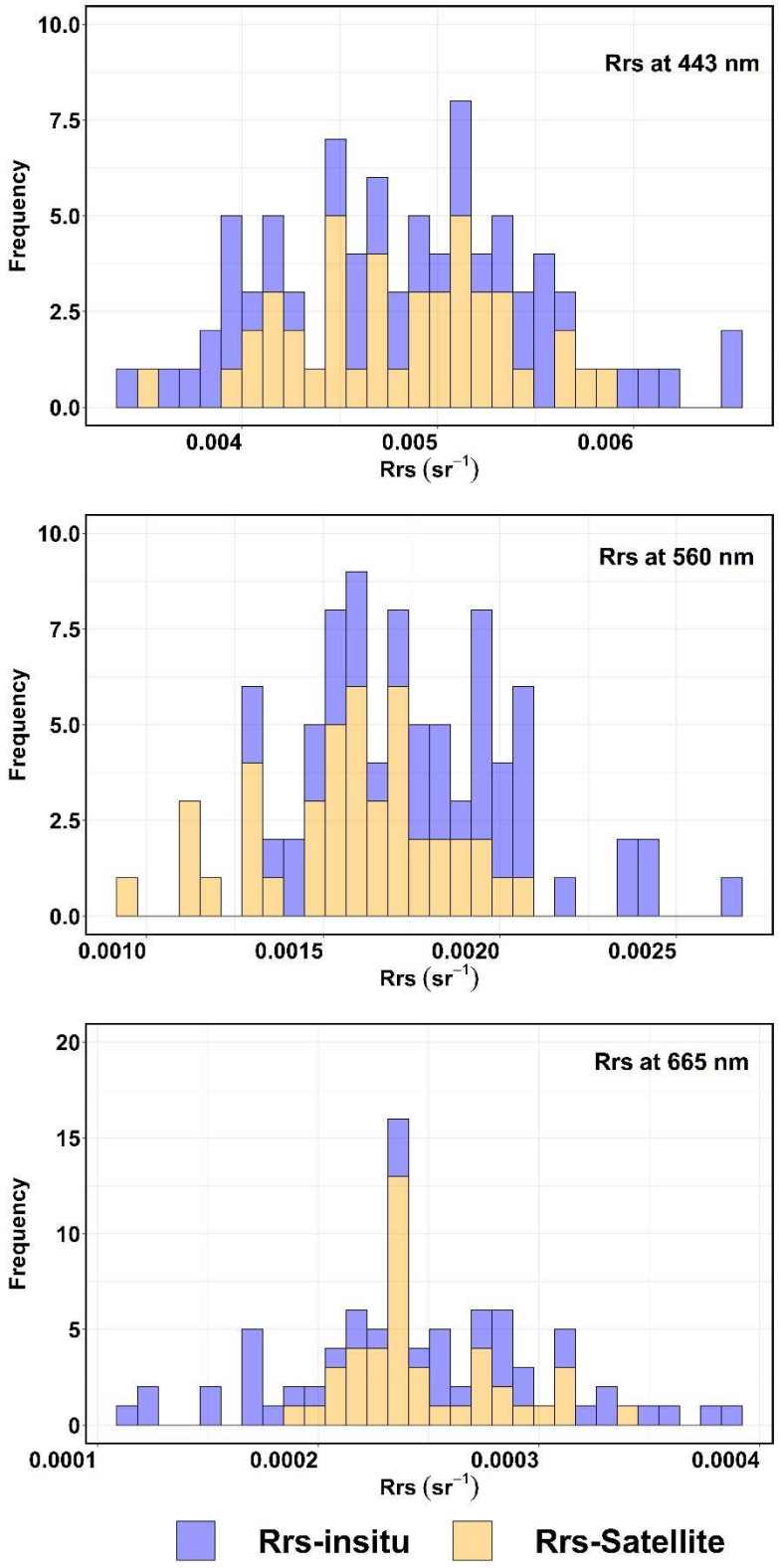

Figure 3. The histogram illustrates the simulated remote sensing reflectance spectra (Rrs in situ) at 443, 555, and 665 nm as well as the corresponding OLCI remote sensing reflectance spectra (Rrs satellite).

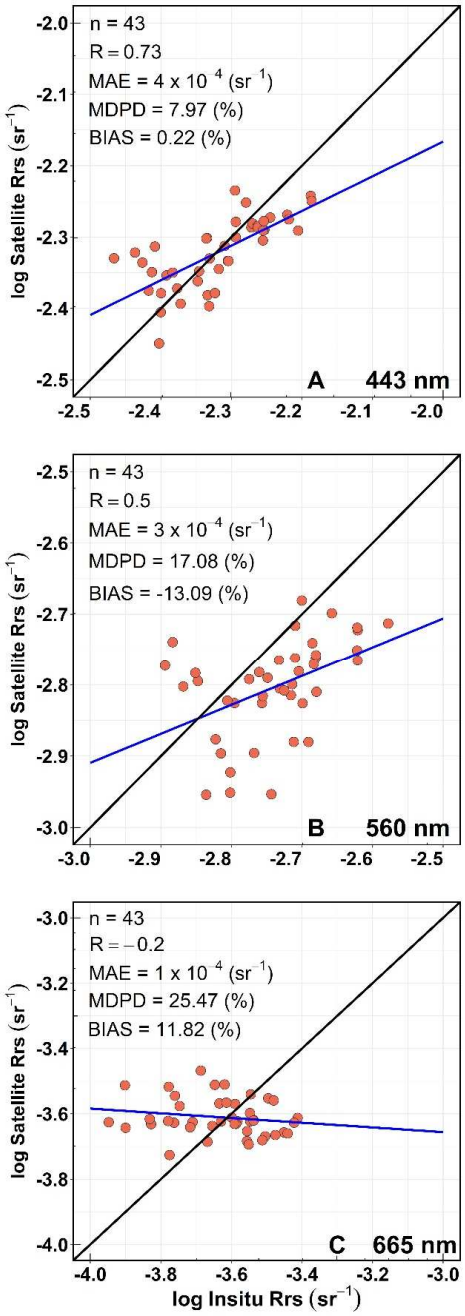

Figure 4. Regression between in situ (*x*-axis) versus satellite-derived (*y*-axis) remote sensing reflectance at 443, 560, and 665 nm. The black line represents the 1:1 line, and the colored line is the linear regression fit for the atmospheric correction algorithm. Satellite Rrs represents the median value from the 5 × 5 pixel-window.

3.2. Chlorophyll-a Matchup Analysis

The dynamic range of in situ and OLCI-derived Chla corresponds to typical conditions for the region [46]. The in situ Chla ranged from 0.17 to 0.52 mg/m^3 (0.35 ± 0.08 mg/m^3) (Figure 5), while the satellite-derived Chla ranged from 0.21 to 0.59 mg/m^3 (0.38 ± 0.08 mg/m^3) (Figure 5). One-to-one matchup analysis (Figure 6) showed excellent agreement between in situ and satellite-derived Chla (r = 0.78, MAE = 0.05 mg/m^3, MDPD = 9.67%, BIAS = 10.38%; Figure 6). This indicates the ability of the Polymer AC algorithm to retrieve Chla concentration within the expected range for this region. However, a slight overestimation of in situ Chla concentration by Polymer was noted in the range between 0.17 and 0.28 mg/m^3. The matchup analysis showed that, except for a few points, most of the points fall close to the 1:1 line,

indicating a strong correlation between in situ and satellite-derived Chla, which results in better statistical metrics (Figure 6). Therefore, the matchup analysis noted a low MDPD (9.67%) and BIAS (10.38%). At the same time, MAE depends on the concentration, which was comparatively lower (MAE = 0.05 mg/m^3).

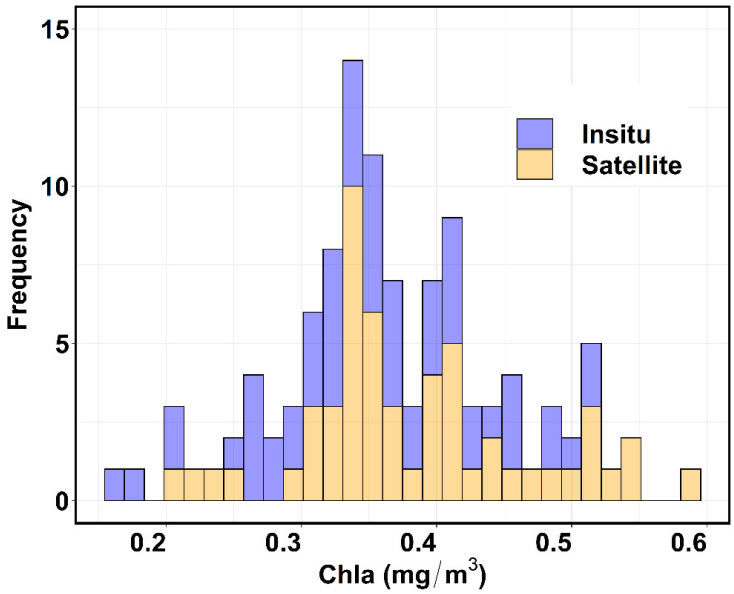

Figure 5. Histogram showing the in situ chlorophyll-a concentration and the corresponding satellite-derived chlorophyll-a concentration for the combined dataset of 2019 and 2020.

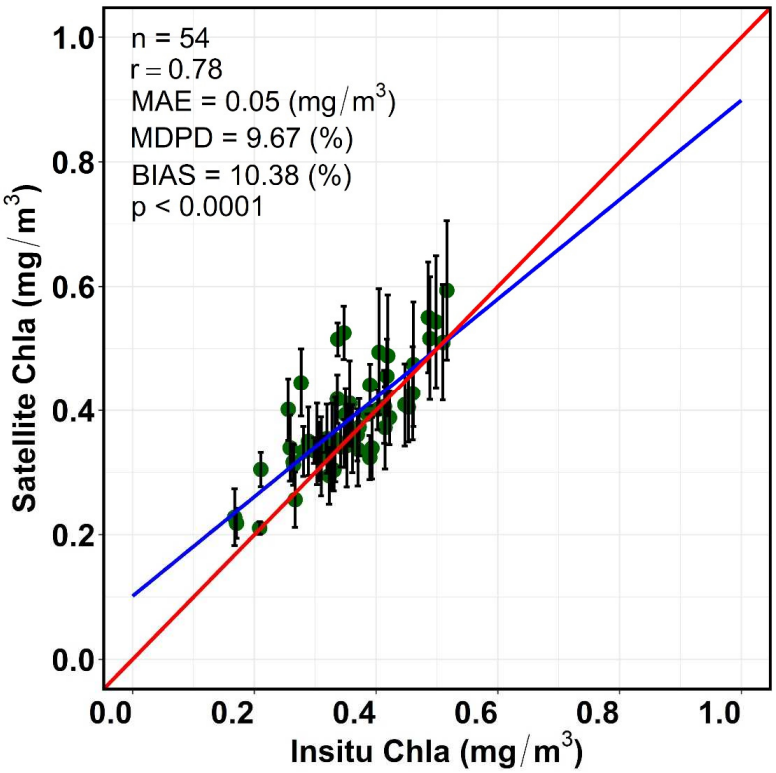

Figure 6. The comparison between in situ versus satellite-derived chlorophyll-a concentration for the combined dataset of 2019 and 2020. The red line shows the 1:1 line and the blue line is the linear regression fit for Chla derived from the Polymer atmospheric correction algorithm. The standard deviation of valid pixels within a 5 × 5-pixel window centered on the location of the in situ observation is represented by vertical bars.

3.3. Spatial Variability of Sentinel-3A OLCI-Derived Chlorophyll-a

The quality of the satellite-derived Chla was further evaluated to determine its ability to capture the known pattern of surface Chla in SNEP over a spatial–temporal domain. Overall, the weekly composites indicated the spatially homogeneous distribution of surface Chla concentration in the iron-poor open ocean waters of GoA (Figure 7). Temporally, the average Chla from the two expeditions remained almost invariant (avg < 0.6 mg/m^3; Figure 7) throughout the region, with values ranging from 0.3 to 0.7 mg/m^3. In addition, no clear spring bloom signal was noticeable in this region. However, intermittent patches of moderate Chla values (>0.6 mg/m^3) were observed within each weekly composite. On the other hand, a substantial increase in concentration ($\geq$0.7 mg/m^3) was recorded toward SEA and the BC coast (Figure 8). For example, the latitudinal trend of Chla derived from each week (Figure 8) showed elevated Chla at 57°N. Similarly, Chla derived from the longitudinal transect also indicated a consistently high value toward −135°W throughout the weeks.

Spatially, regions of high Chla concentration and pronounced seasonal spring blooms were observed along the coast from 2019 to 2020 (Figure 7). For instance, patches of elevated Chla concentrations were marked in northern and SEA, the east coast of Haida Gwaii, and the west coast of Vancouver Island. In the 2019 composites, high Chla concentration patches were defined in the third week of February (18 to 25 February), mainly along northern and SEA, the east coast of Haida Gwaii, northern Vancouver Island, and the west coast of Vancouver Island. Regions of high Chla concentration persisted during the final week of February (26 February to 5 March 2019), with wider spatial distribution mainly along northern and SEA, the east coast of Haida Gwaii, the north and west coast of Vancouver Island, and the Strait of Georgia (SoG), with the highest recorded Chla of 5.8 mg/m^3. Similarly, localized regions of high Chla concentration with larger spatial dispersion were prominent along the west coast from the second (6 to 13 March 2019) to the third (13 to 21 March 2019) weeks of March, with the highest recorded Chla of 6.9 mg/m^3 observed during the third week of March.

On the other hand, during the first week of March 2020 (5–12 March), high Chla concentrations were observed in multiple regions, including SEA, the east coast of Haida Gwaii, the west coast of Vancouver Island, and SoG, with a peak Chla concentration of 6.6 mg/m^3. However, in the third week (13–20 March), a more extensive distribution of high Chla regions was noted, exhibiting a pattern similar to that observed during the first week. Additionally, the highest Chla value (8.9 mg/m^3) among the four composites was recorded that week. Subsequently, from the fourth week of March (21–28 March) to the first week of April (29 March–5 April), a widespread distribution of high Chla values was observed along the coast from SEA to the BC coast. Furthermore, the highest Chla concentrations recorded during the fourth week of March and the first week of April were at 8.0 and 8.3 mg/m^3, respectively.

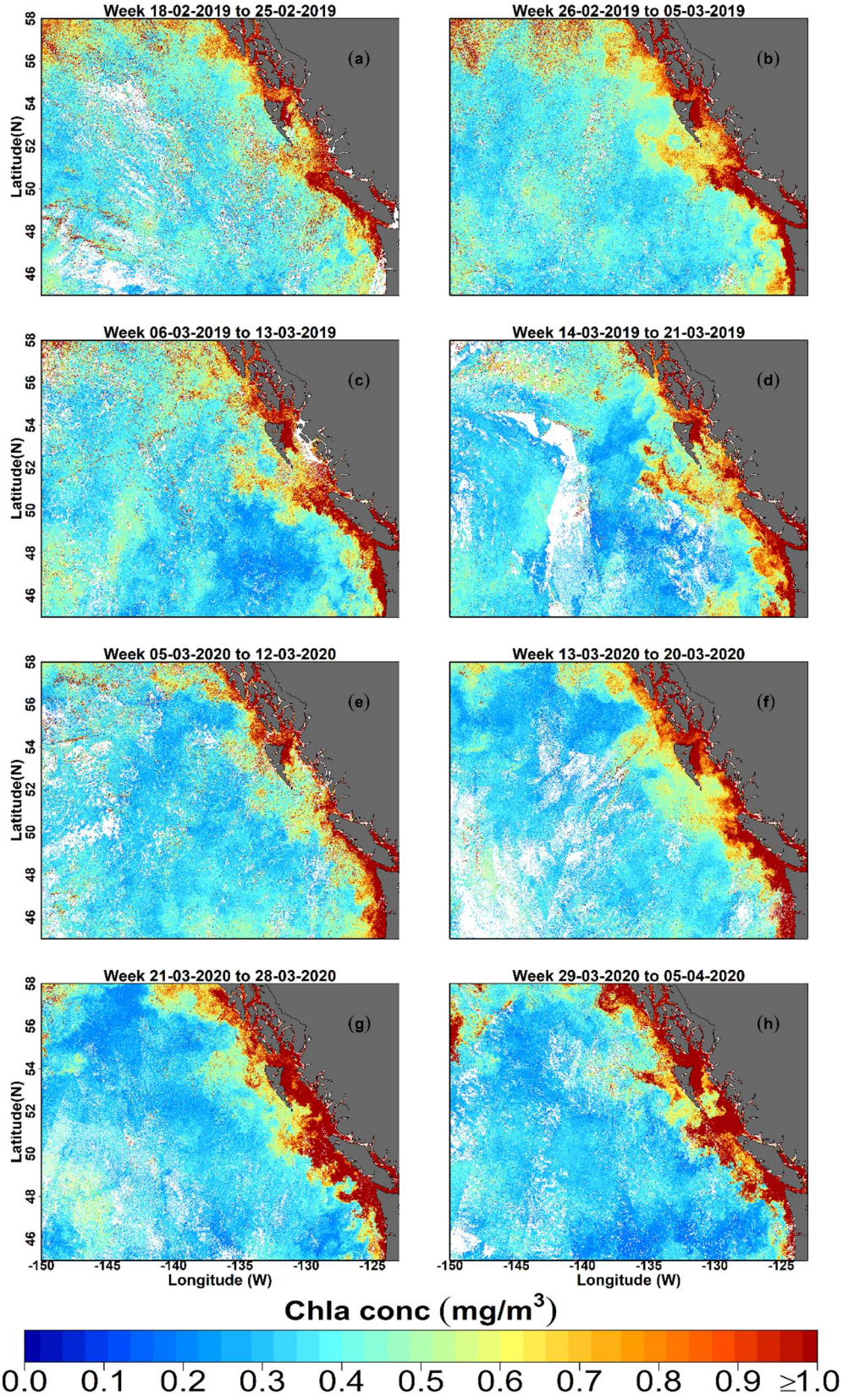

Figure 7. Spatial distribution of the weekly binned surface chlorophyll-a concentration over the subarctic northeast Pacific for 2019 and 2020. (**a**–**d**) spatially and temporally binned surface chlorophyll-a for the week of 18 February 2019 to 21 March 2019. (**e**–**h**) spatially and temporally binned surface chlorophyll-a for the week of 5 March 2020 to 5 April 2020. White regions in the map represent clouds.

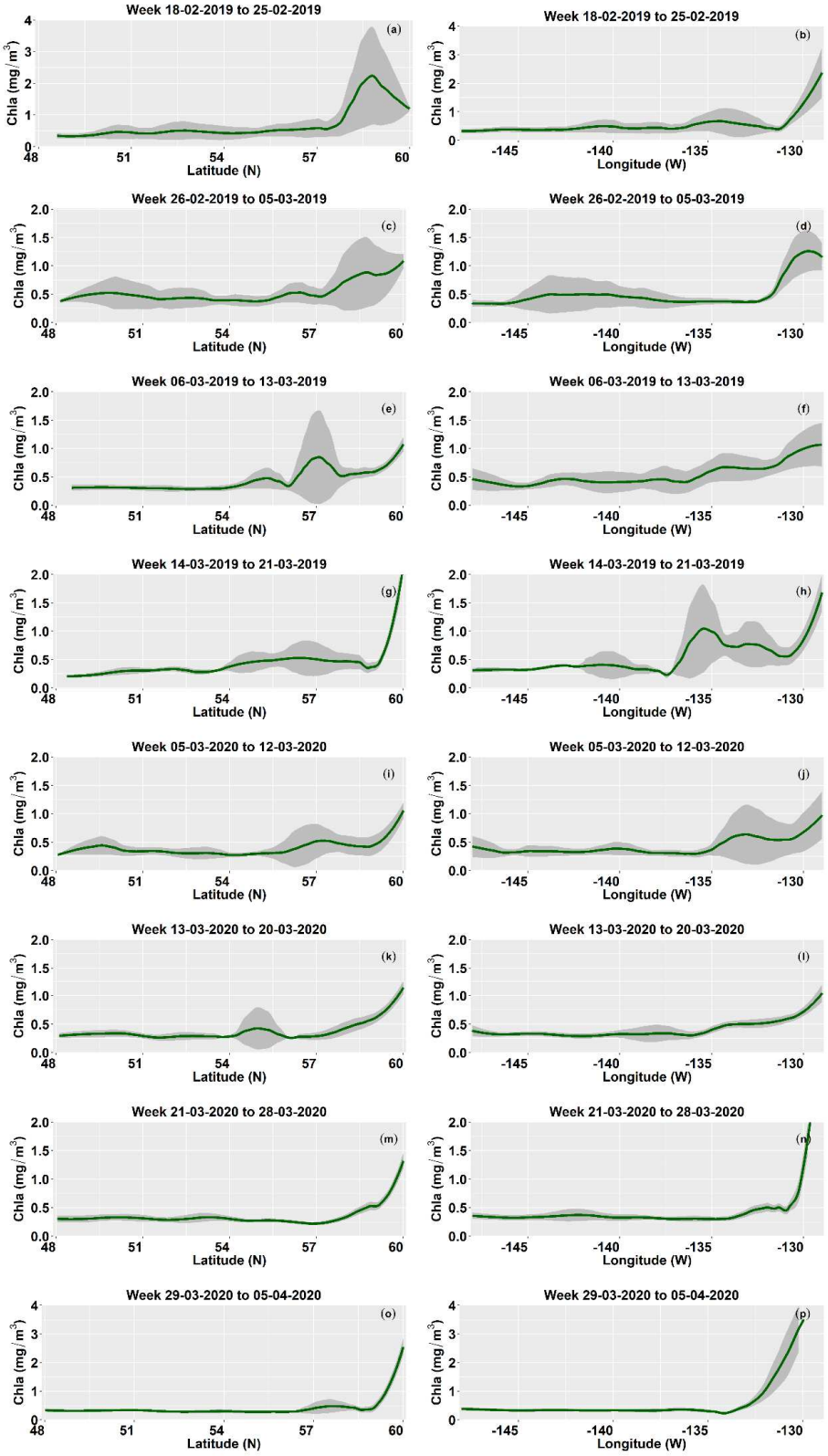

Figure 8. Latitudinal and longitudinal distribution of surface chlorophyll-a concentration extracted from each weekly composite imagery for 2019 and 2020. The Chla concentration is extracted from a 5 × 5-pixel window, and the standard deviation is plotted as a gray-shaded region. (**a**–**h**) latitudinal and longitudinal distribution of surface chlorophyll-a for the week of 18 February 2019 to 21 March 2019. (**i**–**p**) latitudinal and longitudinal distribution of surface chlorophyll-a for the week of 5 March 2020 to 5 April 2020. The corresponding longitudinal and latitudinal lines are displayed in Figure 1.

4. Discussion

This study provides the first validation of Sentinel-3 OLCI Rrs(λ) and Chla products in relation to in situ measurements of the SNEP region. The validation results of the Rrs satellite revealed superior radiometric performance for the blue and green bands and inferior performance for the red band. However, excellent agreement between in situ and satellite-derived Chla concentration was demonstrated in Chla validation. Furthermore, satellite-derived weekly Chla composites displayed relatively low (<0.5 mg/m^3) and spatially homogenous distribution in the ion-poor open ocean waters, while elevated Chla values were ($\geq$0.7 mg/m^3) observed toward SEA and BC. The following sections present the analysis of our main findings.

4.1. Evaluation of the Satellite-Derived Products

4.1.1. Remote Sensing Reflectance

We evaluated the ability of the Polymer AC algorithm to retrieve Rrs satellite for determining Chla in the SNEP using Rrs in situ and Chla data. Our findings indicate that Rrs satellite and Rrs in situ follow spectrally similar shapes and have highly comparable average values, indicating the ability of Polymer AC schemes to derive Rrs in optically Case-1-type water. Additionally, the validation effort to determine the retrieval accuracy of Polymer AC demonstrated that retrievals improved with decreasing wavelength. For example, Polymer showed better radiometric performance in the blue and green spectral regions, whereas an inferior radiometric performance was obtained in the red region (Figure 4). Moreover, the Polymer slightly over- and underestimated Rrs values between 0.0012 and 0.0018 sr^{-1} in the green band, whereas it fails to represent Rrs in situ in the red band. In their latest study, Tilstone et al. 2021 [70] observed that the residual error in Polymer-derived Rrs values varies across different spectral bands, with relatively low mean residual error at the blue (6%) and green (15%) bands, followed by high mean residual error at the red band (60%), which is consistent with our observation. This variation in residual error is likely due to imperfections in AC and uncertainty of in situ measurements. For instance, satellite sensors often detect weak signals at longer wavelengths, such as at 560 and 665 nm from clear Case-1 waters [75]; thus, AC remains highly challenging in this region compared to other spectral regions, eventually leading to over- and underestimation of the lower reflectance values [76,77]. Until now, there has been no established method to remove the residual error from satellite-derived Rrs, which for the clear open ocean waters is observed to be more pronounced in the red band, accounting for up to 60%, followed by the green band (15%) [70]. Consistent with the above findings, the latest study by Gilerson et al. 2022 [76] assessed uncertainties in satellite-derived Rrs from the open ocean and found the highest CV of 1.5–2.0 in the red band compared to the blue band.

Beyond the performance of satellite-derived products, the quality of in situ data is crucial for the accurate validation of satellite data. However, in situ data carry substantial uncertainty for multiple reasons, including inherent sensor noise combined with experimental and environmental factors [57,58,78–81]. For instance, uncertainties in above-water radiometry can arise from sensor calibration, ship shadow and superstructure, environmental conditions, and parameterization of sky glint [58]. Nevertheless, strict guidelines are followed to acquire high-quality radiometric measurements, such as regarding the use of calibrated sensors, performing data collection only during solar noon conditions, and a setup to eliminate ship shadow and superstructure [57,58]. According to a recent study, environmental variability (e.g., wind speed, sun zenith, sky condition, wave height, and sunglint) is the primary source of uncertainty across all wavelengths (410, 490, 550, and 620 nm), accounting for up to 80% of the total [82], wherein the environmental variability, sky condition, wind speed, and the sun zenith angle contribute to the highest uncertainty [82]. In our study, despite conducting data acquisition during solar noon, we encountered several days with overcast conditions during the cruise, which could have contributed considerable uncertainty to the Rrs(λ) measurements. This has been documented in a recent study, which found that uncertainties of up to 80% can occur in the blue

(410 and 490 nm) and green (550 nm) bands and up to 60% in the red band (620 nm) under overcast conditions [82]. These conditions, characterized by scattered clouds and limited sun illumination, cause substantial variability in sunlight, leading to significant deviations in sky radiance (Li(λ)) [82]. In addition, total radiance (Lt(λ)) is also affected, as it receives a significant amount of reflectance from different parts of the sky, and its measurements can be unpredictable due to variations in wave height over time [82]. Finally, radiometric measurements were also affected by the viewing and illumination geometry, which can be addressed by correction for bidirectional effects (BRDF) [83]. Therefore, it is important to take caution and follow strict guidelines while acquiring high-quality in situ radiometry data for validating OC products.

4.1.2. Chlorophyll-a Concentration

Despite OLCI slightly overestimating lower-range Chla values (0.17 to 0.28 mg/m^3) in comparison to in situ measurements, the validation results demonstrate the excellent performance of the Polymer AC algorithm in this region, with dynamic ranges consistent with in situ values [50]. Our observation is supported by Giannini et al. (2021) [62], who evaluated the performance of Polymer and other AC schemes in the northeast Pacific region and found that Polymer provided the best results for Chla and that the dynamic range was within the observed range [39]. This finding is also substantiated by Marchese et al. (2002) [50], who showed that the monthly climatology of Chla derived from OLCI using Polymer recorded low biomass ($\leq$0.5 mg/m^3) in offshore waters of Alaska. Similar to these findings, Tilstone et al. (2021) [70] found that Polymer is the most promising AC processor for retrieving Chla concentration between 0.01 and 1.00 mg/m^3 across the oligotrophic Atlantic Gyre, particularly under thin clouds and sunglint, which may affect the Chla retrieval.

Nonetheless, the slight discrepancy observed between satellite and in situ-derived Chla values may arise from multiple sources. For instance, in our study, the satellite data typically represent the median value within the 5 × 5-pixel window extracted from weekly composite imagery, whereas in situ data represent point location. Satellite matchups using weekly composite extracted from a 5 × 5-pixel window are accepted in oligotrophic waters due to the low variability in phytoplankton biomass within 1500 × 1500 m spatial resolution [73]. This is relevant for the SNEP because of only subtle variability in the phytoplankton community of central Alaska compared to those of the highly dynamic SEA and BC shelf regions [53]. Furthermore, we also found that spatial–temporal mismatch might not have played a substantial role, as we did not observe any notable difference between the average values of satellite-derived Chla from the weekly composite (0.38 ± 0.08 mg/m^3) versus the daily imagery (0.39 ± 0.08 mg/m^3). Another potential discrepancy arises from the tendency of satellite-based measurements to generally overestimate the surface Chla values when a deep chlorophyll maximum (DCM) is present [84]. In a recent study, it was found that Chla values integrated over the first optical depth are 30% higher than surface values [84], which is relevant for the SNEP, where a recent study recorded maximum Chla values of 0.35 mg/m^3 below the mixed layer depth [85].

Beyond the performance of the atmospheric correction algorithm, the validation performance was impacted by the uncertainty associated with the analytical quality of in situ HPLC pigment measurements. Despite the widespread use of HPLC-derived Chla for the validation of satellite-derived Chla [86], these measurements are often subject to multiple sources of errors [87]. For instance, a round-robin experiment conducted by Claustre et al. 2004 [88] using multiple HPLC methods to quantify the uncertainty budget revealed a 7% error for Chla and a 21% error for other pigments. In this study, the overall uncertainty associated with the HPLC pigment data, including sampling methods, filtration, extraction, and HPLC analysis, based on evaluating duplicates of samples, resulted in a CV lower than 20%. However, as in many studies [88,89], it is difficult to quantify any remaining source of error attributed to the in situ Chla measurements.

4.2. Spatial–Temporal Dynamics of Phytoplankton Biomass

Although matchup statistics were obtained, the evaluation of the overall quality of satellite-derived Chla remains challenging due to the sources of uncertainty. Here, we further assessed the quality of the derived Chla products by comparing the latitudinal and longitudinal gradient from weekly composite imagery with the previous literature. The satellite-derived Chla concentration showed the expected low concentration (<0.5 mg/m^3) in the iron-poor open ocean region, with no prominent variability observed between weeks, and the average Chla value was well within the range reported for satellite observations [49,53]. However, intermittent patches of moderate Chla (>0.5 mg/m^3) values were also observed in our imagery. Our findings are consistent with recent satellite observations, demonstrating that Chla concentration in the iron-poor Alaska waters remained low ($\leq$0.4 mg/m^3) throughout the year [40], with an annual mean peak occurring only by fall [6]. Again, low temporal variability in the upper Chla concentration was reported in this region without apparent seasonal or interannual variability [39,46]. These findings were confirmed by the latest observation using the Biogeochemical Argo float (BGC-Argo), which indicated less variability in Chla concentration in the upper 150 m, consistent with the satellite observation [40]. As an HNLC region, iron primarily governs the bloom dynamics, and iron limitation restricts the occurrence of diatom bloom, which is a common phenomenon for the shelf region [89]. Another reason for the low Chla concentration in this region is the strong coupling between the phytoplankton and zooplankton communities, where the latter effectively grazes on the former, resulting in a relatively constant Chla concentration throughout the year [90].

Unlike the open waters, our weekly composite maps showed high Chla concentrations (i.e., between 5.4 and 8.9 mg/m^3) and pronounced spring bloom signals along SEA to the BC coast (Figure 7). Consistent with our findings, previous studies reported relatively high Chla levels (>3.0 mg/m^3) along with pronounced spring bloom characterized by marked seasonal, spatial, and interannual variability in this region [6,7,27]. The latest satellite-based observations also substantiate these findings by recording high spring average Chla (>2.0 mg/m^3) across SEA to the BC coast [49,50,54].

Generally, our composite imagery from 2019 displayed a greater spatial extent in Chla concentration along the coast from the last week of February to the third week of March. Conversely, the imagery from 2020 revealed a larger spatial extent of higher Chla concentration along the coast from the second week of March to the second week of April. These findings are consistent with recent satellite-based observations of the BC coast, which have found that, in terms of timing, the spring bloom along the west coast of Vancouver typically starts in March [49,54,89]. The latest study using high spatial and temporal resolution satellite imagery found that the seasonal increase in average Chla concentration across SEA to the BC coast region is between late February and early April [50], consistent with our findings. In addition, our weekly composite imagery revealed regions of high Chla values during spring, which were concentrated in northern and SEA, the east coast of Haida Gwaii, and along the north, south, and west coasts of Vancouver Island, as well as in the SoG. These zones were identified as bioregions in the northeast Pacific, confirming our findings and demonstrating that they are characterized by high Chla values (>2.4 mg/m^3) and exhibit an annual peak in spring [50]. The mechanism by which elevated Chla levels and spring blooms are sustained across SEA and the BC shelf is attributed to several processes, including iron-rich coastal freshwater runoff, strong upwelling, tidal mixing, high levels of irradiance, the lengthening of daylight hours, and stratification of the water column [7,13,16,26,90–93].

5. Conclusions

In this study, we aimed to investigate the performance of Sentinel-3A OC products, specifically Rrs(λ) and Chla concentrations, against in situ data. Additionally, we conducted a qualitative assessment with reference to previous studies to determine whether the weekly binned surface Chla concentration reflects the general latitudinal and longitudinal trends in this region. The in situ and satellite-derived Rrs(λ) revealed a Case-1 water spectrum

with maximum reflectance in the blue band that exponentially decreased toward longer wavelengths, followed by Chla fluorescence at 680 nm. The validation of the Rrs satellite against Rrs in situ showed there was a good correlation and better statistical performance in the blue and green regions, with a degraded performance recorded in the red band. Moreover, Polymer tends to overestimate or underestimate Rrs levels in the green band, specifically within the range of 0.0012 to 0.0018 sr^{-1}, where POLYMER fails to represent the Rrs in the red bands. Chla matchup analysis showed excellent agreement between in situ and satellite-derived Chla. Furthermore, Polymer slightly overestimates the lower ranges of in situ Chla from 0.17 to 0.28 mg/m^3. The spatial and temporal dynamics of weekly binned surface Chla maps show low biomass in the iron-poor open ocean water; however, a substantial increase in Chla ($\geq$0.7 mg/m^3) was recorded toward the SEA and BC shelf. Furthermore, the latitudinal and longitudinal distribution of Chla reveals high biomass toward 57°N and −135°W, respectively.

High spatial and temporal resolution Chla maps are essential for this region to better understand the dynamics of surface phytoplankton, which are the foundation of the marine food web. Malick et al. 2015 [94] reported that the spring bloom phenology in the northeast Pacific Ocean is significantly correlated with Pacific salmon productivity in Alaska and BC. Similarly, Suchy et al. 2022 [95] demonstrated the connection between phytoplankton bloom dynamics and zooplankton phenology in the coastal waters of BC, revealing that early and late spring blooms result in mismatches between phytoplankton and zooplankton phenology, with implications for the food web. In this context, our findings could help fishery management by providing spatial and temporal data on phytoplankton bloom in the SNEP region, where Pacific salmon spend most of their adult life [17], enabling the better management of fishery resources across this region. In addition, our study represents the first attempt to utilize high spatial (300 m) and temporal (daily) resolution satellite imagery to validate Sentinel-3 OLCI products in the undersampled oligotrophic region of the SNEP. The results show the potential of OLCI to retrieve the OC products as well as the spatial–temporal pattern of Chla concentration over a synoptic scale, which would not be possible otherwise.

Author Contributions: Conceptualization, P.S.V. and M.C.; methodology, P.S.V.; validation, P.S.V.; formal analysis, P.S.V.; investigation, P.S.V.; resources, M.C.; data curation, P.S.V.; writing—original draft preparation, P.S.V.; writing—review and editing, P.S.V. and M.C.; visualization, P.S.V.; supervision, M.C.; project administration, M.C.; funding acquisition, M.C. All authors have read and agreed to the published version of the manuscript.

Funding: This research was funded by the NSERC NCE MEOPAR—Marine Environmental Observation, Prediction, and Response Network and the Canadian Space Agency (FAST 18FAVICB09). We would also like to acknowledge the International Year of Salmon for providing payment-in-kind financial support for the fieldwork.

Data Availability Statement: Data are available upon request.

Acknowledgments: We would like to acknowledge Richard Beamish, Brian Riddell, and the NPAFC secretariat for organizing the 2019 and 2020 Gulf of Alaska expeditions. The authors would like to thank the scientific members, technicians, and crew members of the research vessels *Professor Kaganovsky* and *Pacific Legacy* for their help and assistance during the expeditions. We thank sound engineer Igor Pankov for helping with the above-water radiometry operation during the 2019 expedition. The authors also thank Natalie Mahara and Jacob Lerner for collecting the water samples and performing filtration for HPLC pigments during the 2020 expedition.

Conflicts of Interest: The authors declare no conflict of interest.

References

1. Field, C.B.; Behrenfeld, M.J.; Randerson, J.T.; Falkowski, P. Primary Production of the Biosphere: Integrating Terrestrial and Oceanic Components. *Science* **1998**, *281*, 237–240. [CrossRef]
2. Le Quere, C.; Harrison, S.P.; Prentice, I.C.; Buitenhuis, E.T.; Aumont, O.; Bopp, L.; Claustre, H.; Da Cunha, L.C.; Geinder, R.; Giraud, X.; et al. Ecosystem Dynamics Based on Plankton Functional Types for Global Ocean Biogeochemistry Models. *Glob. Chang. Biol.* **2005**, *11*, 2016–2040. [CrossRef]
3. Falkowski, P. Ocean Science: The Power of Plankton. *Nature* **2012**, *483*, S17–S20. [CrossRef] [PubMed]
4. Bouman, H.A.; Ulloa, O.; Scanlan, D.J.; Zwirglmaier, K.; Li, W.K.W.; Platt, T.; Stuart, V.; Barlow, R.; Leth, O.; Clementson, L.; et al. Oceanographic Basis of the Global Surface Distribution of Prochlorococcus Ecotypes. *Science* **2006**, *312*, 918–921. [CrossRef] [PubMed]
5. Miller, C.B.; Frost, B.W.; Wheeler, P.A.; Landry, M.R.; Welschmeyer, N.; Powell, T.M.; Limnology, S.; Phytoplankton, W.C.; Miller, C.B.; Frost, B.W.; et al. Ecological Dynamics in the Subarctic Pacific, A Possibly Iron-Limited Ecosystem. *Limnol. Oceanogr.* **1991**, *36*, 1600–1615. [CrossRef]
6. Brickley, P.J.; Thomas, A.C. Satellite-Measured Seasonal and Inter-Annual Chlorophyll Variability in the Northeast Pacific and Coastal Gulf of Alaska. *Deep. Sea Res. Part II Top. Stud. Oceanogr.* **2004**, *51*, 229–245. [CrossRef]
7. Strom, S.L.; Fredrickson, K.A.; Bright, K.J. Spring Phytoplankton in the Eastern Coastal Gulf of Alaska: Photosynthesis and Production during High and Low Bloom Years. *Deep. Sea Res. Part II Top. Stud. Oceanogr.* **2016**, *132*, 107–121. [CrossRef]
8. Evans, G.T.; Parslow, J.S. A Model of Annual Plankton Cycles. *Biol. Oceanogr.* **1985**, *3*, 327–347. [CrossRef]
9. McClain, C.R. A Decade of Satellite Ocean Color Observations. *Annu. Rev. Mar. Sci.* **2009**, *1*, 19–42. [CrossRef]
10. Hamme, R.C.; Webley, P.W.; Crawford, W.R.; Whitney, F.A.; Degrandpre, M.D.; Emerson, S.R.; Eriksen, C.C.; Giesbrecht, K.E.; Gower, J.F.R.; Kavanaugh, M.T.; et al. Volcanic Ash Fuels Anomalous Plankton Bloom in Subarctic Northeast Pacific. *Geophys. Res. Lett.* **2010**, *37*, 1–5. [CrossRef]
11. Frost, B.W. The Role of Grazing in Nutrient-rich Areas of the Open Sea. *Limnol. Oceanogr.* **1991**, *36*, 1616–1630. [CrossRef]
12. Banse, K.; English, D.C. Comparing Phytoplankton Seasonality in the Eastern and Western Subarctic Pacific and the Western Bering Sea. *Prog. Oceanogr.* **1999**, *43*, 235–288. [CrossRef]
13. Harrison, P.J.; Boyd, P.W.; Varela, D.E.; Takeda, S.; Shiomoto, A.; Odate, T. Comparison of Factors Controlling Phytoplankton Productivity in the NE and NW Subarctic Pacific Gyres. *Prog. Oceanogr.* **1999**, *43*, 205–234. [CrossRef]
14. Bishop, J.K.B.; Davis, R.E.; Sherman, J.T. Robotic Observations of Dust Storm Enhancement of Carbon Biomass in the North Pacific. *Science* **2002**, *298*, 817–821. [CrossRef]
15. Harris, S.L.; Varela, D.E.; Whitney, F.W.; Harrison, P.J. Nutrient and Phytoplankton Dynamics off the West Coast of Vancouver Island during the 1997/98 ENSO Event. *Deep. Sea Res. Part II Top. Stud. Oceanogr.* **2009**, *56*, 2487–2502. [CrossRef]
16. Marchetti, A.; Juneau, P.; Whitney, F.A.; Wong, C.S.; Harrison, P.J. Phytoplankton Processes during a Mesoscale Iron Enrichment in the NE Subarctic Pacific: Part II-Nutrient Utilization. *Deep. Sea Res. Part II Top. Stud. Oceanogr.* **2006**, *53*, 2114–2130. [CrossRef]
17. Beamish, R.J. What the Past Tells Us about the Future of Pacific Salmon Research. *Fish Fish.* **2017**, *18*, 1161–1175. [CrossRef]
18. Siddon, E.C.; De Forest, L.G.; Blood, D.M.; Doyle, M.J.; Matarese, A.C. Early Life History Ecology for Five Commercially and Ecologically Important Fish Species in the Eastern and Western Gulf of Alaska. *Deep. Sea Res. Part II Top. Stud. Oceanogr.* **2019**, *165*, 7–25. [CrossRef]
19. Womble, J.N.; Sigler, M.F. Seasonal Availability of Abundant, Energy-Rich Prey Influences the Abundance and Diet of a Marine Predator, the Steller Sea Lion Eumetopias Jubatus. *Mar. Ecol. Prog. Ser.* **2006**, *325*, 281–293. [CrossRef]
20. Womble, J.N.; Sigler, M.F.; Willson, M.F. Linking Seasonal Distribution Patterns with Prey Availability in a Central-Place Forager, the Steller Sea Lion. *J. Biogeogr.* **2009**, *36*, 439–451. [CrossRef]
21. Johnson, S.W.; Neff, A.D.; Thedinga, J.F.; Lindeberg, M.R.; Maselko, J.M. *Atlas of Nearshore Fishes of Alaska: A Synthesis of Marine Surveys from 1998 to 2011*; NOAA Technical Memorandum NMFS-AFSC-239; U.S. Department of Commerce: Washington, DC, USA, 2012; 261p.
22. McGowan, D.W.; Horne, J.K.; Parker-Stetter, S.L. Variability in Species Composition and Distribution of Forage Fish in the Gulf of Alaska. *Deep. Sea Res. Part II Top. Stud. Oceanogr.* **2019**, *165*, 221–237. [CrossRef]
23. Budge, S.M.; Wang, S.W.; Ormseth, O.A.; Rand, K.M. Foraging Ecology of Nearshore Fishes in the Gulf of Alaska. *Deep. Sea Res. Part II Top. Stud. Oceanogr.* **2022**, *195*, 105013. [CrossRef]
24. Dragoo, D.E.; Renner, H.M.; Kaler, R.S.A. *Breeding Status, Population Trends and Diets of Seabirds in Alaska, 2016*; U.S. Fish and Wildlife Service Report AMNWR 2017/06; Alaska Maritime National Wildlife Refuge: Homer, Alaska, 2017.
25. Sambrotto, R.N.; Lorenzen, C.J. *The Gulf of Alaska: Physical Environment and Biological Resources*; Hood, D.W., Zimmerman, S.T., Eds.; Ocean Assessments Division, NOAA. U.S. Department of Commerce: Washington, DC, USA, 1987; pp. 249–282, ISBN 0080432077.
26. Childers, A.R.; Whitledge, T.E.; Stockwell, D.A. Seasonal and Interannual Variability in the Distribution of Nutrients and Chlorophyll a across the Gulf of Alaska Shelf: 1998–2000. *Deep. Sea Res. Part II Top. Stud. Oceanogr.* **2005**, *52*, 193–216. [CrossRef]
27. Waite, J.N.; Mueter, F.J. Spatial and Temporal Variability of Chlorophyll-a Concentrations in the Coastal Gulf of Alaska, 1998–2011, Using Cloud-Free Reconstructions of SeaWiFS and MODIS-Aqua Data. *Prog. Oceanogr.* **2013**, *116*, 179–192. [CrossRef]
28. Stabeno, P.J.; Bond, N.A.; Hermann, A.J.; Kachel, N.B.; Mordy, C.W.; Overland, J.E. Meteorology and Oceanography of the Northern Gulf of Alaska. *Cont. Shelf Res.* **2004**, *24*, 859–897. [CrossRef]

29. Olson, R.J.; Sosik, H.M. A Submersible Imaging-in-Flow Instrument to Analyze Nano-and Microplankton: Imaging FlowCytobot. *Limnol. Oceanogr. Methods* **2007**, *5*, 195–203. [CrossRef]
30. Lombard, F.; Boss, E.; Waite, A.M.; Uitz, J.; Stemmann, L.; Sosik, H.M.; Schulz, J.; Romagnan, J.-B.; Picheral, M.; Pearlman, J.; et al. Globally Consistent Quantitative Observations of Planktonic Ecosystems. *Front. Mar. Sci.* **2019**, *6*, 1–21. [CrossRef]
31. Harrison, P.J.; Whitney, F.A.; Tsuda, A.; Saito, H.; Tadokoro, K. Nutrient and Plankton Dynamics in the NE and NW Gyres of the Subarctic Pacific Ocean. *J. Oceanogr.* **2004**, *60*, 93–117. [CrossRef]
32. Booth, B.C.; Lewin, J.; Postel, J.R. Temporal Variation in the Structure of Autotrophic and Heterotrophic Communities in the Subarctic Pacific. *Prog. Oceanogr.* **1993**, *32*, 57–99. [CrossRef]
33. Peterson, T.D.; Harrison, P.J. Diatom Dynamics in a Long-Lived Mesoscale Eddy in the Northeast Subarctic Pacific Ocean. *Deep. Sea Res. Part I Oceanogr. Res. Pap.* **2012**, *65*, 157–170. [CrossRef]
34. Obayashi, Y.; Tanoue, E.; Suzuki, K.; Handa, N.; Nojiri, Y.; Wong, C.S. Spatial and Temporal Variabilities of Phytoplankton Community Structure in the Northern North Pacific as Determined by Phytoplankton Pigments. *Deep. Sea Res. Part I Oceanogr. Res. Pap.* **2001**, *48*, 439–469. [CrossRef]
35. Suzuki, K.; Minami, C.; Liu, H.; Saino, T. Temporal and Spatial Patterns of Chemotaxonomic Algal Pigments in the Subarctic Pacific and the Bering Sea during the Early Summer of 1999. *Deep. Sea Res. Part II Top. Stud. Oceanogr.* **2002**, *49*, 5685–5704. [CrossRef]
36. Fujiki, T.; Matsumoto, K.; Honda, M.C.; Kawakami, H.; Watanabe, S. Phytoplankton Composition in the Subarctic North Pacific during Autumn 2005. *J. Plankton Res.* **2009**, *31*, 179–191. [CrossRef]
37. Peterson, T.D.; Crawford, D.W.; Harrison, P.J. Evolution of the Phytoplankton Assemblage in a Long-Lived Mesoscale Eddy in the Eastern Gulf of Alaska. *Mar. Ecol. Prog. Ser.* **2011**, *424*, 53–73. [CrossRef]
38. Yang, B.; Emerson, S.R.; Penã, M.A. The Effect of the 2013–2016 High Temperature Anomaly in the Subarctic Northeast Pacific (the "Blob") on Net Community Production. *Biogeosciences* **2018**, *15*, 6747–6759. [CrossRef]
39. Peña, M.A.; Nemcek, N.; Robert, M. Phytoplankton Responses to the 2014–2016 Warming Anomaly in the Northeast Subarctic Pacific Ocean. *Limnol. Oceanogr.* **2019**, *64*, 515–525. [CrossRef]
40. Zhang, H.; Wang, Y.; Xiu, P.; Chai, F. Modeling the Seasonal Variability of Phytoplankton in the Subarctic Northeast Pacific Ocean. *Mar. Ecol. Prog. Ser.* **2021**, *680*, 33–50. [CrossRef]
41. Sathyendranath, S.; Aiken, J.; Alvain, S.; Barlow, R.; Bouman, H.; Bracher, A.; Brewin, R.J.W.; Bricaud, A.; Brown, C.W.; Ciotti, A.M.; et al. *Phytoplankton Functional Types from Space*; Report of the International Ocean-Colour Coordinating Group (IOCCG), 15; International Ocean-Colour Coordinating Group: Dartmouth, NS, Canada, 2014.
42. Vinogradov, M.E.; Shushkina, E.A.; Vedernikov, V.I.; Nezlin, N.P.; Gagarin, V.I. Primary Production and Plankton Stocks in the Pacific Ocean and Their Seasonal Variation According to Remote Sensing and Field Observations. *Deep. Sea Res. Part II Top. Stud. Oceanogr.* **1997**, *44*, 1979–2001. [CrossRef]
43. EUMETSAT. *Sentinel-3 OLCI Marine User Handbook 2018*; EUMETSAT: Darmstadt, Germany, 2018; ISBN 4961518077.
44. Weingartner, T. *The Physical Environment of the Gulf of Alaska*, 1st ed.; Spies, R.B., Ed.; Elsevier: Amsterdam, The Netherlands, 2006; ISBN 9780444529602.
45. Weingartner, T.; Eisner, L.; Eckert, G.L.; Danielson, S. Southeast Alaska: Oceanographic Habitats and Linkages. *J. Biogeogr.* **2009**, *36*, 387–400. [CrossRef]
46. Peña, M.A.; Varela, D.E. Seasonal and Interannual Variability in Phytoplankton and Nutrient Dynamics along Line P in the NE Subarctic Pacific. *Prog. Oceanogr.* **2007**, *75*, 200–222. [CrossRef]
47. Zhang, H.R.; Wang, Y.; Xiu, P.; Qi, Y.; Chai, F. Roles of Iron Limitation in Phytoplankton Dynamics in the Western and Eastern Subarctic Pacific. *Front. Mar. Sci.* **2021**, *8*, 735826. [CrossRef]
48. Welschmeyer, N.A.; Strom, S.; Goericke, R.; DiTullio, G.; Belvin, M.; Petersen, W. Primary Production in the Subarctic Pacific Ocean: Project SUPER. *Prog. Oceanogr.* **1993**, *32*, 101–135. [CrossRef]
49. Westberry, T.K.; Schultz, P.; Behrenfeld, M.J.; Dunne, J.P.; Hiscock, M.R.; Maritorena, S.; Sarmiento, J.L.; Siegel, D.A. Annual Cycles of Phytoplankton Biomass in the Subarctic Atlantic and Pacific Ocean. *Glob. Biogeochem. Cycles* **2016**, *30*, 175–190. [CrossRef]
50. Marchese, C.; Hunt, B.P.V.; Giannini, F.; Ehrler, M.; Costa, M. Bioregionalization of the Coastal and Open Oceans of British Columbia and Southeast Alaska Based on Sentinel-3A Satellite-Derived Phytoplankton Seasonality. *Front. Mar. Sci.* **2022**, *9*, 968470. [CrossRef]
51. Weingartner, T.J.; Danielson, S.L.; Royer, T.C. Freshwater Variability and Predictability in the Alaska Coastal Current. *Deep. Sea Res. Part II Top. Stud. Oceanogr.* **2005**, *52*, 169–191. [CrossRef]
52. Thomson, R.E.; Beamish, R.J.; Beacham, T.D.; Trudel, M.; Whitfield, P.H.; Hourston, R.A.S. Anomalous Ocean Conditions May Explain the Recent Extreme Variability in Fraser River Sockeye Salmon Production. *Mar. Coast. Fish. Dyn. Manag. Ecosyst. Sci.* **2012**, *4*, 415–437. [CrossRef]
53. Jackson, J.M.; Thomson, R.E.; Brown, L.N.; Willis, P.G.; Borstad, G.A. Satellite Chlorophyll off the British Columbia Coast, 1997–2010. *J. Geophys. Res. Ocean.* **2015**, *120*, 4709–4728. [CrossRef]
54. Peterson, T.D.; Toews, H.N.J.; Robinson, C.L.K.; Harrison, P.J. Nutrient and Phytoplankton Dynamics in the Queen Charlotte Islands (Canada) during the Summer Upwelling Seasons of 2001–2002. *J. Plankton Res.* **2007**, *29*, 219–239. [CrossRef]

55. Mueller, J.L.; Bidigare, R.R.; Trees, C.; Balch, W.M.; Dore, J.; Drapeau, D.T.; Karl, D.M.; Van Heukelem, L.; Perl, J. Ocean Optics Protocols for Satellite Ocean Color Sensor Validation, Revision 5: Biogeochemical and Bio-Optical Measurements and Data Analysis Protocols. Mueller, J.L., Fargion, G.S., McClain, C.R., Eds.; Goddard Space Flight Space Center: Greenbelt, MD, USA, 2003; Volume 5.
56. Pinckney, J.L. The USC Method. In *The Fourth SeaWiFS HPLC Analysis Round-Robin Experiment (SeaHARRE-4)*; NASA: Washington, DC, USA, 2010.
57. Mobley, C.D. Estimation of the Remote-Sensing Reflectance from above-Surface Measurements. *Appl. Opt.* **1999**, *38*, 7442–7455. [CrossRef]
58. Hooker, S.B.; Morel, A. Platform and Environmental Effects on Above-Water Determinations of Water-Leaving Radiances. *J. Atmos. Ocean. Technol.* **2003**, *20*, 187–205. [CrossRef]
59. Ruddick, K.; De Cauwer, V.; Van Mol, B. Use of the Near Infrared Similarity Reflectance Spectrum for the Quality Control of Remote Sensing Data. In *Remote Sensing of the Coastal Oceanic Environment*; Society of Photo-optical Instrumentation Engineers: Bellingham, WA, USA, 2005; p. 588501.
60. Ruddick, K.G.; De Cauwer, V.; Park, Y.-J.; Moore, G. Seaborne Measurements of Near Infrared Water-Leaving Reflectance: The Similarity Spectrum for Turbid Waters. *Limnol. Oceanogr.* **2006**, *51*, 1167–1179. [CrossRef]
61. Donlon, C.; Berruti, B.; Buongiorno, A.; Ferreira, M.-H.; Féménias, P.; Frerick, J.; Goryl, P.; Klein, U.; Laur, H.; Mavrocordatos, C.; et al. The Global Monitoring for Environment and Security (GMES) Sentinel-3 mission. *Remote Sens. Environ.* **2012**, *120*, 37–57. [CrossRef]
62. Giannini, F.; Hunt, B.P.V.; Jacoby, D.; Costa, M. Performance of OLCI Sentinel-3A Satellite in the Northeast Pacific Coastal Waters. *Remote Sens. Environ.* **2021**, *256*, 112317. [CrossRef]
63. Steinmetz, F.; Deschamps, P.-Y.; Ramon, D. Atmospheric Correction in Presence of Sun Glint: Application to MERIS. *Opt. Express* **2011**, *19*, 9783–9800. [CrossRef] [PubMed]
64. Steinmetz, F.; Ramon, D.; Deschamps, P.-Y. ATBD v1—Polymer Atmospheric Correction Algorithm Ref: D2.3 Date: 23/12/2016 Issue: 2.1. PML, United Kingdom 2016. Available online: https://docs.pml.space/share/s/M05k8Lw3QLeXSIiA3X87UQ (accessed on 10 April 2023).
65. Scott, J.P.; Werdell, P.J. Comparing Level-2 and Level-3 Satellite Ocean Color Retrieval Validation Methodologies. *Opt. Express* **2019**, *27*, 30140–30157. [CrossRef] [PubMed]
66. EUMETSAT. REF: SOLVO/EUM/16/VCA/D8. ISSUE: 1.3. July 2017. In *Sentinel-3 OLCI Marine User Handbook*; EUMETSAT: Darmstadt, Germany, 2017.
67. Antoine, D.; Morel, A. A Multiple Scattering Algorithm for Atmospheric Correction of Remotely Sensed Ocean Colour (MERIS Instrument): Principle and Implementation for Atmospheres Carrying Various Aerosols Including Absorbing Ones. *Int. J. Remote Sens.* **1999**, *20*, 1875–1916. [CrossRef]
68. Moore, G.F.; Aiken, J.; Lavender, S.J. The Atmospheric Correction of Water Colour and the Quantitative Retrieval of Suspended Particulate Matter in Case II Waters: Application to MERIS. *Int. J. Remote. Sens.* **1999**, *20*, 1713–1733. [CrossRef]
69. Moore, G.F.; Mazeran, C.; Huot, J.P. Case II.S Bright Pixel Atmospheric Correction. *Eur. Space Agency* **2017**, *5*.
70. Tilstone, G.H.; Pardo, S.; Dall'Olmo, G.; Brewin, R.J.W.; Nencioli, F.; Dessailly, D.; Kwiatkowska, E.; Casal, T.; Donlon, C. Performance of Ocean Colour Chlorophyll a Algorithms for Sentinel-3 OLCI, MODIS-Aqua and Suomi-VIIRS in open-ocean waters of the Atlantic. *Remote Sens. Environ.* **2021**, *260*, 112444. [CrossRef]
71. Hijmans, R.J. Raster: Geographic Data Analysis and Modeling. 2020. Available online: https://CRAN.R-project.org/package=raster (accessed on 22 January 2022).
72. Mograne, M.A.; Jamet, C.; Loisel, H.; Vantrepotte, V.; Mériaux, X.; Cauvin, A. Evaluation of Five Atmospheric Correction Algorithms over French Optically-Complex Waters for the Sentinel-3A OLCI Ocean Color Sensor. *Remote Sens.* **2019**, *11*, 668. [CrossRef]
73. Bailey, S.W.; Werdell, P.J. A Multi-Sensor Approach for the on-Orbit Validation of Ocean Color Satellite Data Products. *Remote Sens. Environ.* **2006**, *102*, 12–23. [CrossRef]
74. Pramlall, S.; Jackson, J.M.; Konik, M.; Costa, M. Merged Multi-Sensor Ocean Colour Chlorophyll Product Evaluation for the British Columbia Coast. *Remote Sens.* **2023**, *15*, 687. [CrossRef]
75. Hu, C.; Feng, L.; Lee, Z. Uncertainties of SeaWiFS and MODIS Remote Sensing Reflectance: Implications from Clear Water Measurements. *Remote Sens. Environ.* **2013**, *133*, 168–182. [CrossRef]
76. Gilerson, A.; Herrera-Estrella, E.; Foster, R.; Agagliate, J.; Hu, C.; Ibrahim, A.; Franz, B. Determining the Primary Sources of Uncertainty in Retrieval of Marine Remote Sensing Reflectance From Satellite Ocean Color Sensors. *Front. Remote. Sens.* **2022**, *3*, 1–19. [CrossRef]
77. Zibordi, G.; Ruddick, K.; Ansko, I.; Moore, G.; Kratzer, S.; Icely, J.; Reinart, A. In Situ Determination of the Remote Sensing Reflectance: An Inter-Comparison. *Ocean Sci.* **2012**, *8*, 567–586. [CrossRef]
78. Vabson, V.; Kuusk, J.; Ansko, I.; Vendt, R.; Alikas, K.; Ruddick, K.; Ansper, A.; Bresciani, M.; Burmester, H.; Costa, M.; et al. Laboratory Intercomparison of Radiometers Used for Satellite Validation in the 400–900 nm Range. *Remote Sens.* **2019**, *11*, 1101. [CrossRef]
79. Vabson, V.; Kuusk, J.; Ansko, I.; Vendt, R.; Alikas, K.; Ruddick, K.; Ansper, A.; Bresciani, M.; Burmester, H.; Costa, M.; et al. Field Intercomparison of Radiometers Used for Satellite Validation in the 400–900 nm Range. *Remote Sens.* **2019**, *11*, 1129. [CrossRef]

80. Ruddick, K.G.; Voss, K.; Banks, A.C.; Boss, E.; Castagna, A.; Frouin, R.; Hieronymi, M.; Jamet, C.; Johnson, B.C.; Kuusk, J.; et al. A Review of Protocols for Fiducial Reference Measurements of Downwelling Irradiance for the Validation of Satellite Remote Sensing Data over Water. *Remote Sens.* **2019**, *11*, 1742. [CrossRef]
81. Tilstone, G.; Dall'Olmo, G.; Hieronymi, M.; Ruddick, K.; Beck, M.; Ligi, M.; Costa, M.; D'Alimonte, D.; Vellucci, V.; Vansteenwegen, D.; et al. Field Intercomparison of Radiometer Measurements for Ocean Colour Validation. *Remote Sens.* **2020**, *12*, 1587. [CrossRef]
82. Lin, J.; Dall'Olmo, G.; Tilstone, G.H.; Brewin, R.J.W.; Vabson, V.; Ansko, I.; Evers-King, H.; Casal, T.; Donlon, C. Derivation of Uncertainty Budgets for Continuous Above-Water Radiometric Measurements along an Atlantic Meridional Transect. *Opt. Express* **2022**, *30*, 45648–45675. [CrossRef]
83. Morel, A.; Gentili, B. Diffuse Reflectance of Oceanic Waters III Implication of Bidirectionality for the Remote-Sensing Problem. *Appl. Opt.* **1996**, *35*, 4850–4862. [CrossRef] [PubMed]
84. Sá, C.; D'Alimonte, D.; Brito, A.C.; Kajiyama, T.; Mendes, C.R.; Vitorino, J.; Oliveira, P.B.; da Silva, J.C.B.; Brotas, V. Validation of Standard and Alternative Satellite Ocean-Color Chlorophyll Products off Western Iberia. *Remote Sens. Environ.* **2015**, *168*, 403–419. [CrossRef]
85. Meyer, M.G.; Gong, W.; Kafrissen, S.M.; Torano, O.; Varela, D.E.; Santoro, A.E.; Cassar, N.; Gifford, S.; Niebergall, A.K.; Sharpe, G.; et al. Phytoplankton Size-Class Contributions to New and Regenerated Production during the EXPORTS Northeast Pacific Ocean Field Deployment. *Elem. Sci. Anthr.* **2022**, *10*, 00068. [CrossRef]
86. Bracher, A.; Bouman, H.A.; Brewin, R.J.W.; Bricaud, A.; Brotas, V.; Ciotti, A.M.; Clementson, L.; Devred, E.; Di Cicco, A.; Dutkiewicz, S.; et al. Obtaining Phytoplankton Diversity from Ocean Color: A Scientific Roadmap for Future Development. *Front. Mar. Sci.* **2017**, *4*, 1–15. [CrossRef]
87. Van Heukelem, L.; Hooker, S.B. The Importance of a Quality Assurance Plan for Method Validation and Minimizing Uncertainties in the HPLC Analysis of Phytoplankton Pigments. In *Phytoplankton pigments: Characterization, Chemotaxonomy, and Applications in Oceanography*; Suzanne, R., Llewellyn, C.A., Egeland, E.S., Ohnsen, G., Eds.; Cambridge University Press: Cambridge, UK, 2011; pp. 195–242, ISBN 978-1-107-00066-7.
88. Claustre, H.; Hooker, S.B.; Van Heukelem, L.; Berthon, J.-F.; Barlow, R.; Ras, J.; Sessions, H.; Targa, C.; Thomas, C.S.; Van Der Linde, D.; et al. An Intercomparison of HPLC Phytoplankton Pigment Methods Using in Situ Samples: Application to Remote Sensing and Database Activities. *Mar. Chem.* **2004**, *85*, 41–61. [CrossRef]
89. Ribalet, F.; Marchetti, A.; Hubbard, K.A.; Brown, K.; Durkin, C.A.; Morales, R.; Robert, M.; Swalwell, J.E.; Tortell, P.D.; Armbrust, E.V. Unveiling a Phytoplankton Hotspot at a Narrow Boundary between Coastal and Offshore Waters. *Proc. Natl. Acad. Sci. USA* **2010**, *107*, 16571–16576. [CrossRef]
90. Landry, M.R.; Monger, B.C.; Selph, K.E. Time-Dependency of Microzooplankton Grazing and Phytoplankton Growth in the Subarctic Pacific. *Prog. Oceanogr.* **1993**, *32*, 205–222. [CrossRef]
91. Suchy, K.D.; Le Baron, N.; Hilborn, A.; Perry, R.I.; Costa, M. Influence of Environmental Drivers on Spatio-Temporal Dynamics of Satellite-Derived Chlorophyll a in the Strait of Georgia. *Prog. Oceanogr.* **2019**, *176*, 102134. [CrossRef]
92. Strom, S.L.; Olson, M.B.; Macri, E.L.; Mordy, C.W. Cross-Shelf Gradients in Phytoplankton Community Structure, Nutrient Utilization, and Growth Rate in the Coastal Gulf of Alaska. *Mar. Ecol. Prog. Ser.* **2006**, *328*, 75–92. [CrossRef]
93. Henson, S.A. Water Column Stability and Spring Bloom Dynamics in the Gulf of Alaska. *J. Mar. Res.* **2007**, *65*, 715–736. [CrossRef]
94. Malick, M.J.; Cox, S.P.; Mueter, F.J.; Peterman, R.M. Linking Phytoplankton Phenology to Salmon Productivity along a North-South Gradient in the Northeast Pacific Ocean. *Can. J. Fish. Aquat. Sci.* **2015**, *72*, 697–708. [CrossRef]
95. Suchy, K.D.; Young, K.; Galbraith, M.; Perry, R.I.; Costa, M. Match/Mismatch Between Phytoplankton and Crustacean Zooplankton Phenology in the Strait of Georgia, Canada. *Front. Mar. Sci.* **2022**, *9*, 1–21. [CrossRef]